# Tomographic reconstruction of light field PIV based on backward ray-tracing technique

**IOP** Publishing Journal Title
Journal **XX** (XXXX) XXXXXX https://doi.org/XXXX/XXXX

# Tomographic Reconstruction of Light Field PIV Based on Backward Ray-Tracing Technique

**Lixia Cao[1], Biao Zhang[1], MD. Moinul Hossain[2], Jian Li[1], Chuanlong Xu[1,*]**

[1]National Engineering Research Center of Turbo-Generator Vibration, School of Energy and Environment, Southeast University, Nanjing 210096, China
[2]School of Engineering and Digital Arts, University of Kent, Canterbury, Kent, CT2 7NT, UK
*Correspondent author: chuanlongxu@seu.edu.cn

Received xxxxxx
Accepted for publication xxxxxx
Published xxxxxx

## Abstract

The calculation of the weight matrix is one of the key steps of the tomographic reconstruction in the light field particle image velocimetry (light field PIV) system. At present, the existing calculation method of the weight matrix in light field PIV based on the forward ray-tracing technique (named as Fahringer's method) is very time-consuming. To improve the computational efficiency of the weight matrix, this paper presents a computational method for the weight matrix based on the backward ray-tracing technique in combination with Gaussian function (named as Gaussian function method). An Expectation-Maximization (EM) algorithm is employed for the reconstruction of the 3D particle field, and a summed line-of-sight (SLOS) estimation is further used to accelerate the reconstruction process. The computational accuracy and efficiency of the weight matrix, the reconstruction quality of the 3D particle field, and the velocity field accuracy by Gaussian function method are numerically investigated. Finally, experiments are carried out to verify the feasibility of the weight matrix by Gaussian function method. Numerical results illustrated that Gaussian function method can improve the computational efficiency of the weight matrix by more than 10 times. SLOS is capable of further accelerating the computational efficiency of the overall reconstruction process including the pre-determination, the calculation of the weight matrix and the reconstruction. The velocity field accuracy by Gaussian function method is almost the same as that by Fahringer's method. The experimental results of the 3D-3C velocity field of a laminar flow further verify the feasibility of the computational method for the weight matrix based on Gaussian function.

Keywords: weight matrix, tomographic reconstruction, particle image velocimetry, backward ray-tracing technique, light field imaging

## 1. Introduction

Most problems in fluid dynamics are involved with complex, three-dimensional (3D) and unsteady flows such as the turbulent flow, flow in boundary layer and spray [1-3]. The 3D velocity field plays a crucial role in characterizing the 3D structure of various complex flows [4]. An accurate and efficient measurement of the 3D velocity field helps to reveal the topology and nature of various complex flows, which is useful for the optimized operation and design of fluid mechanics [5]. Three-dimensional and three-component (3D-3C) particle image velocimetry (PIV) technique is capable of achieving the measurement of 3D-3C velocity field and has the advantages of non-intrusiveness and instantaneity, and has become an important means for the characterization of the topologies of various 3D unsteady and complicated flow structures [6].

The tomographic PIV (Tomo-PIV) is one of the most useful experimental methods for measurement and characterization of the 3D-3C velocity field due to its advantages of high spatial resolution and being suitable for the volumetric velocity measurement at different scales [7-10]. In Tomo-PIV, the measurement volume is captured by the conventional multi-cameras system (usually three or more conventional cameras) [11]. The Algebraic reconstruction technique (ART) and the multiplicative algebraic reconstruction technique (MART) are usually used for the reconstruction of the 3D particle field. The synthetic aperture PIV (SA-PIV) is a computationally cheap and effcient 3D-3C PIV technique, and its experimental setup is very similar to the Tomo-PIV [12-13]. The SA-PIV is implemented by a camera array similar to the light field imaging system distributed in the measurement volume from different views. The multiple 2D refocused planes at various depths throughout the entire measurement volume are reconstructed by the refocusing algorithm. The particles with lower intensities in the 2D refocused planes are removed when their intensities are lower than a set threshold. The SA-PIV is capable of obtaining the 3D particle field. Furthermore, the refocusing algorithm in the SA-PIV is more efficient than MART and ART in the Tomo-PIV. However, in the SA-PIV, eight or more conventional cameras are usually required to record the tracer particles seeded in the measurement volume from different views [14]. Thus, the multi-cameras system of the SA-PIV is more complex and expensive than that of the Tomo-PIV. This results in a complex coupling and synchronization of the multiple-cameras so that the operation and mounting of the multiple-cameras PIV system is inconvenient for the complex flow mechanics [15-16], especially for the space-constraint applications such as the 3D measurement of high-temperature and high-pressure turbulent flow in internal engine. As an alternative to the multi-cameras PIV, the light field PIV based on a single light field camera has received much attention recently [17-20]. Compared with the conventional camera, a microlens array (MLA) is mounted in front of the CCD sensor in the light field camera so that the direction and the position of the light field can be simultaneously recorded in a single exposure [21-22]. So a single light field camera is capable of capturing the tracer particles in the flow field instead of the multi-cameras system in the Tomo-PIV and SA-PIV. This uniqueness greatly simplifies the Tomo-PIV and SA-PIV system for the 3D flow measurement. Presently, many research works on the light field PIV have been performed for the measurement of the instantaneous velocity field. Skupsch *et al*. proposed the SA-PIV based on a single light field camera to measure the velocity field of the flow field [23]. In this work, the multi-light sheets with constant spacing were used to illuminate the flow field instead of the volumetric illumination. The refocused planes at the position of the multi-light sheets were reconstructed by the refocusing algorithm. Then, the deblurring algorithm was used to remove the particles with lower intensities in the 2D refocused planes. The 2D cross-correlation was used for the calculation of the velocity field in each refocused plane. Skupsch's SA-PIV based on a single light field camera is a 2D-3C PIV technique.

Brian Thurow's group of Auburn university [17-18] firstly proposed a Tomo-PIV technique based on a single light field camera and achieved the measurement of the 3D-3C velocity field. Since then, Brian Thurow's group has carried out a lot of research works on the light field PIV for the measurement of the 3D-3C velocity field of the flow field, and many progresses have been made recently. Bolton *et al*. used a single light field camera to measure the shock wave-turbulent boundary layer interaction, and proven that the light field camera was capable of obtaining the 3D velocity information of the supersonic flows [24]. Thomason studied the calibration of the plenoptic camera based on the focal point method and the magnification method [25]. His thesis proved that the magnification method could provide a reasonable estimation for the image distance, and the focal point method is limited by the error when a complex lens is assumed to be a thin lens in the real application. The focal point method is capable of providing a comparable accuracy to the magnification method by using a correction equation. Munz *et al*. proposed a volumetric calibration based on a 3D polynomial mapping function to calibrate the light field camera, and corrected errors due to the lens distortion and thin lens assumption [26]. The volumetric calibration was capable of directly achieving the image position corresponding to the 3D position in the object space. Fahringer *et al*. used the dual light field cameras to reconstruct the 3D particle field. Their work indicated that the dual light field cameras were capable of mitigating the elongation of the reconstructed particle in the depth, and has a higher reconstruction quality than a single light field camera [27]. However, the computational cost of the weight matrix increases with the increase of the number of cameras.

Shi's group of Shanghai Jiao Tong University has also conducted a lot of research works on the light field PIV. Shi *et al*. [28] studied the effects of the pixel-microlens ratio and MLA geometry on the tomographic reconstruction quality, and his work has verified that the light field PIV was capable of achieving the measurement accuracy level of the flow field similar to the multi-cameras Tomo-PIV when the plenoptic camera resolution is relatively high [29]. In 2019, Shi *et al*. proposed a calibration mode based on Gaussian optics. This method could determine the relationship between a voxel in the object space and its affected microlens and pixels, and the center and diameter of confusion circle produced on microlens array [30]. The distortion caused by the main lens and the misalignments between the MLA and CCD sensor were taken into account. Thus, their calibration method was capable of providing an accurate weight coefficient for the 3D particle reconstruction. In 2020, they further proposed a flexible calibration method for the unfocused plenoptic camera based on the plenoptic type features [31]. They used a 'plenoptic disk features' to operate the raw light-field image. A centroid algorithm was used for the detection of the point-like features related to a point in 3-D space. Their method avoided some intermediate processing steps of generating sub-aperture images and detecting features on these sub-aperture images. Mei *et al*. studied a 3DPIV technique based on a dual light field camera framework [32]. Meanwhile, the influence of the view angle and tracer particle density on the reconstruction quality and spatial resolution were investigated. The comparison of the reconstruction results between a single light field camera and a dual light field camera was conducted. Their method showed that a dual light field camera could mitigate the elongation of reconstructed particles and improve the depth resolution. Meanwhile, Shi *et al*. used a single-camera light-field PIV to measure the velocity field of synthetic jet, self-similar adverse pressure gradient turbulent boundary layer, supersonic jet and turbomachinery blades [33-36].

Cao and Xu *et al*. of Southeast University [37] also studied the effects of the optical parameters of the light field camera on the tomographic reconstruction quality, and further optimized the configuration of the light field camera.

Despite rapid progress and developments in the light field PIV for the measurement of the 3D-3C velocity field, some issues and challenges need to be addressed in the real applications. One of the major issues is the low calculation efficiency of the weight matrix, making the tomographic reconstruction of the light field PIV time-consuming. The weight matrix describes the relationship between the discretized voxels in the measurement volume and their corresponding imaging pixels in the light field camera. The computational efficiency of the weight matrix is closely dependent on the number of the elements of the weight matrix and the calculation method. In the light field PIV, the forward ray-tracing technique is usually used for the calculation of the weight matrix. Through the forward ray-tracing technique, the light rays emitted from the voxel are traced to the main lens, the MLA, and then onto the pixel on the CCD sensor. In Fahringer's works [38], each light ray from the voxel center is assumed to have a certain width equal to a single microlens pitch instead of a point. Thus, for the orthogonal MLA (the center of all microlenses forms an orthogonal grid), each light ray from the voxel center passing through the main lens is almost always received by the 4 microlenses and the 16 pixels beneath these 4 microlenses. This means that the projection of each light ray on the MLA plane is divided into the 4 rectangles by the 4 microlenses, and the 16 rectangles on the pixel plane beneath these 4 microlenses by the 16 pixels. The area of the rectangle is the contribution coefficient. Because of the special geometric relationship, a linear interpolation method is easily used for the calculation of these rectangle areas. However, the linear method is limited to the orthogonal MLA. Additionally, the discretized voxel pitch in the measurement volume should be close to the microlens pitch to ensure the special geometric relationship. The calculation process of the weight matrix takes on the order of 10s of hours even by parallel computation [39]. In Shi's studies [40], the dense light rays from a given voxel are traced onto the MLA plane and the CCD sensor, respectively. The weight coefficient is calculated as the multiplication of the overlap between the dense light rays and the MLA ($w_1$), and the overlap between the light rays and the pixels ($w_2$) [24]. It does not need to consider the geometry of the MLA. However, it is also time-consuming. Different from the forward ray-tracing technique, the backward ray-tracing technique is usually adopted by the conventional Tomo-PIV and traces the light rays from the pixel center to the measurement volume in the flow field [41-43]. The contribution of the voxel to the pixels is dependent on the distance between the voxel and the pixel's line-of-sight, which is characterized by a Gaussian function [44-45]. The light field camera can better represent the light beam sampled by the pixel in direction than the conventional camera [46]. So the backward ray-tracing technique combined with Gaussian function has the potential to provide a simple computational method for the weight matrix in the light field camera to improve its calculation efficiency.

This paper aims to present a computational method based on the backward ray-tracing technique combined with Gaussian function (named as Gaussian function method) to improve the calculation efficiency of the weight matrix in light field PIV. The 3D particle field is reconstructed by an Expectation-Maximization (EM) algorithm. A summed line-of-sight (SLOS) estimation is further used for the optimization of the weight matrix to accelerate the reconstruction process. The computational accuracy and efficiency of the weight matrix, the reconstruction quality of the 3D particle field, and the velocity field accuracy by Gaussian function method and the forward ray-tracing technique (named as Fahringer's method) are numerically compared. Finally, a light field PIV setup is built, and experiments are carried out to verify the feasibility of the weight matrix by Gaussian function method. Numerical and experimental results are presented and analyzed.

## 2. Principle of light field PIV

Fig. 1 shows the schematics of the focused light field camera (FL). From Fig. 1, for the light field camera, when the MLA is mounted in front of the CCD sensor, the light rays are separated by the microlens based on their direction, and then imaged on the CCD sensor underneath the microlens [22]. As a consequence, the direction and position of the light field can be simultaneously recorded by a single light field camera in a single exposure. The light beam (also named as the sphere-cylinder, and marked as the yellow, blue and green part in Fig. 1) represents a collection of the rays collected by a single pixel on the CCD sensor. The angle $\theta$ represents the apex angle of the light beam in the 3D object space, and is used to characterize the ability of a single pixel to collect the rays. The pixel's line-of-sight (marked as the black dotted line in Fig. 1) is a ray that passes through the pixel center, the center of its corresponding microlens, the virtual image plane (VIP), the main lens and the virtual object plane (VOP).

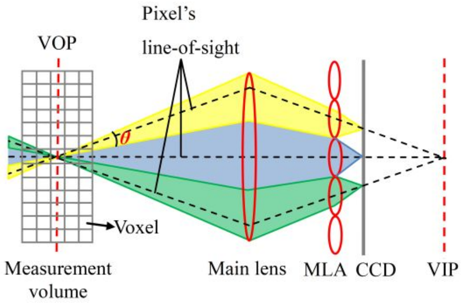


**Fig. 1 Schematics of the focused light field camera (FL)**

For the light field camera, $\theta$ is less than 0.95°, and much smaller than that ($\theta$<6.9°) of the conventional camera at the same optical parameters [46]. This means that the light field camera has the better representative direction than the conventional camera, and the pixels' line-of-sight is more representative of the direction of the light field. So the weight matrix can be calculated by the pixel's line-of-sight in the object space, and then is used for the reconstruction of the 3D particle field.

The light field PIV is schematically shown in Fig. 2. The tracer particles are firstly seeded in the 3D flow region (named as the measurement volume), and then illuminated by a pulse volumetric laser light [9]. The scattered light by the tracer particles at 90° is collected by the light field camera from a single view. Thus, a pair of the light field images of the tracer particles is recorded by the light field camera at the time interval of $\Delta t$, and the 3D tomogram of particle fields are then reconstructed from the light field images. From the 3D tomograms, the particle displacement and the velocity field in the measurement volume are then determined by a 3D cross-correlation technique.

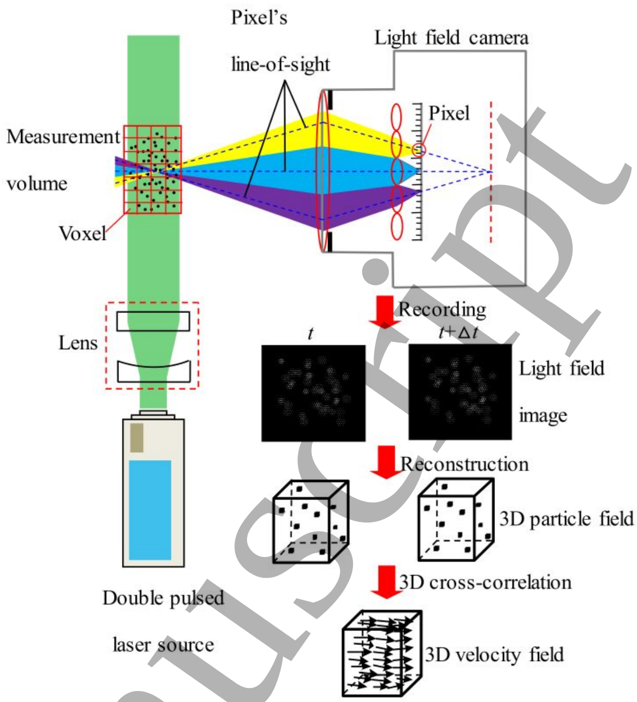


**Fig. 2 Schematic of the light field PIV**

## 3. Reconstruction of light field PIV

### *3.1 Tomographic reconstruction*

The measurement volume is discretized into a 3D array of the cubic voxel with intensity $E$ in the 3D object space. Then, the intensity of each pixel is the integration of the intensity along the pixel's line-of-sight direction $s_i$ in the volume, which is expressed as [47]

$$P_i(x,y)=\int_{S_i}E(X,Y,Z)\,\mathrm{d}s_i \tag{1}$$

where $P_i$ is the intensity recorded by the $i^{\text{th}}$ pixel, $E$ is the intensity of the voxel in the measurement volume. $(x, y)$ is the coordinate of the pixel in the pixel coordinate system, and $(X, Y, Z)$ is the central coordinates of the voxel in the world coordinate system.

Equation (1) is discretized as

$$\begin{bmatrix} P_1 \\ P_2 \\ \vdots \\ P_m \end{bmatrix}=\begin{bmatrix} W_{1,1} & W_{1,2} & \cdots & W_{1,j} & \cdots & W_{1,n} \\ W_{2,1} & W_{2,2} & \cdots & W_{2,j} & \cdots & W_{2,n} \\ \vdots & \vdots & \vdots & \vdots & \vdots & \vdots \\ W_{i,1} & W_{i,2} & \cdots & W_{i,j} & \cdots & W_{i,n} \\ \vdots & \vdots & \vdots & \vdots & \vdots & \vdots \\ W_{m,1} & W_{m,2} & \cdots & W_{m,j} & \cdots & W_{m,n} \end{bmatrix}\begin{bmatrix} E_1 \\ E_2 \\ \vdots \\ E_n \end{bmatrix} \tag{2}$$

where $m$ is the total number of pixels on CCD sensor, $n$ is the total number of the discretized voxels in the measurement volume, and $W_{i,j}$ is the contribution of the $j^{\text{th}}$ voxel to the $i^{\text{th}}$ pixel, which is named as the weight matrix.

The tomographic reconstruction is an inverse process of Equation (2). According to the principle of light field imaging, the light from an object point would affect multiple pixels on the CCD sensor, especially for those further away from the virtual object plane. When the light is spread into more pixels, the corresponding pixel intensity would decrease, and then the pixel intensity would fall below background noise. This is one of the limits of the light field camera. There are two ways to alleviate this limitation. Firstly, a high energy pulsed laser is usually used in 3D-PIV. For the experiments in previous publications and our work, the energy of 200mJ is sufficient for the light field imaging and the measurement of flow field in a certain depth range [18, 39, 41]. Secondly, the robust reconstruction algorithm is used to improve the background noise problem. Among the reconstruction algorithms, deconvolution is usually employed to remove the contributions from out-of-focus objects [48]. It can considerably improve image contrast and reduce noise of image. Expectation-Maximization (EM) algorithm is one of the deconvolution algorithms for a blurred image, which is based on the maximum-likelihood estimate to recover a blurred image. It has a simple iterative scheme, and can quickly converge to a satisfactory solution. In this paper, EM algorithm is used to reconstruct the intensity distribution of the 3D particle field, which is expressed as [49-51]

$$E(X_j,Y_j,Z_j)^{k+1} = E(X_j,Y_j,Z_j)^k \left[ \frac{P_i}{\sum_{j \in N_i} W_{i,j} E(X_j,Y_j,Z_j)^k} W_{i,j} \right] \tag{3}$$

where $k$ is the number of iterations.

The normalized correlation coefficient is used to evaluate the reconstruction quality of the 3D particle field [52],

$$Q = \frac{\sum_j [E_0(X_j,Y_j,Z_j) \cdot E_1(X_j,Y_j,Z_j)]}{\sqrt{\sum_j E_0^2(X_j,Y_j,Z_j) \cdot \sum_j E_1^2(X_j,Y_j,Z_j)}} \tag{4}$$

where $E_0(X_j, Y_j, Z_j)$ and $E_1(X_j, Y_j, Z_j)$ are the real 3D intensity distribution of the $j^{th}$ voxel and the reconstructed 3D intensity distribution of the $j^{th}$ voxel, respectively.

The effect of the particle concentration on the tomographic reconstruction is also studied. The concentration of the tracer particle is defined as the number of particles per each MLA (ppm) [18]

$$P_{con} = \frac{N_{particle}}{N_{microlens}} \tag{5}$$

where $N_{particle}$ and $N_{microlens}$ are the numbers of the tracer particles and the MLAs, respectively.

### *3.2 Calculation of the weight matrix based on the backward ray-tracing*

A backward ray-tracing technique is used to trace the pixel's line-of-sight from the pixel center to the object space. The schematics of the backward ray-tracing technique of the FL are shown in Fig. 3. As shown in Fig. 3, the pixel's line-of-sight passes through the center of the MLA, and then reaches the main lens. The coordinate of the intersection point $A$ between the pixel's line-of-sight and the main lens is calculated by

$$y_1 = m_y - l_m \frac{s_y - m_y}{d_2} \tag{6}$$

where $m_y$ is the central coordinate of the MLA along the $Y$-axis in the world coordinate system, $l_m$ is the distance between the main lens and the MLA, $s_y$ is the central coordinate of the sub-image along the $Y$-axis in the world coordinate system, and $d_2$ is the distance between the MLA and the CCD sensor.

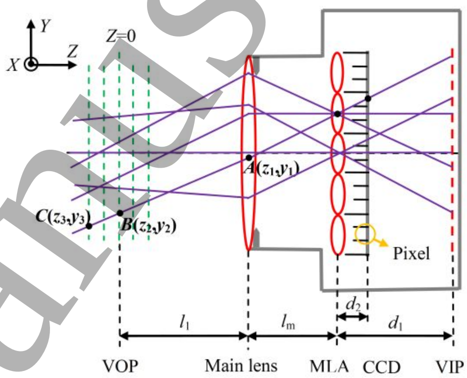


**Fig. 3 Schematics of the backward ray-tracing technique of the FL**

Then, the pixel's line-of-sight passes through the VOP, and the coordinate of intersection point $B$ between the pixel's line-of-sight and the VOP is calculated by

$$y_2 = \frac{-l_1}{l_m + d_1} \cdot \frac{s_y d_1 - m_y d_1 + d_2 m_y}{d_2} \tag{7}$$

where $l_1$ is the distance between the VOP and the main lens, and $d_1$ is the distance between the MLA and the VIP.

Finally, the coordinate of the intersection point $C$ between the pixel's line-of-sight and the arbitrary voxel plane (marked as the green dotted line in Fig. 3) is calculated by

$$y_3 = y_2 - \frac{z_3(y_2 - y_1)}{l_1} \tag{8}$$

where $z_3$ is the distance between the arbitrary voxel plane and the VOP in the $Z$-axis.

For a given $j^{th}$ voxel, $W_{i,j}$ is dependent on its size and the distance between its center and pixel's line-of-sight, and is characterized by Gaussian function [26, 41-42],

$$W_{i,j} = A\mathrm{e}^{-\frac{d_{i,j}^2}{2\sigma^2}}$$

(9)

where $\sigma$ is the standard deviation which is used to characterize the width of Gaussian distribution, and $d_{i,j}$ is the perpendicular distance between the center of the voxel and the pixel's line-of-sight.

From the above analysis, the number of light rays traced by the backward ray-tracing technique is greatly less than that by the forward ray-tracing technique, which is greatly useful to improve compactional efficiency. Besides, the calculation of the weight matrix by Gaussian function method is suitable for both the orthogonal and hexagonal MLA.

## 4.Numerical simulations

Numerical simulations are performed to validate the accuracy and feasibility of the weight matrix by Gaussian function method.

A server with a 32 core Intel (R) Xeon(R) CPU E5-2696 V4@2.2GHz and 128GB RAW is used for the calculations of the weight matrix, the tomographic reconstruction and the 3D cross-correlation. The parameters of the light field camera in Fig. 3 are listed in Table 1. For the convenience, several terms are defined as:

FL-Gaussian-O: Gaussian function method is used for the calculation of the weight matrix in the FL with the orthogonal MLA. FL-Gaussian-H: Gaussian function method is used for the calculation of the weight matrix in the FL with the hexagonal MLA. FL-Gaussian-SLOS: SLOS is used for the optimization of the weight matrix in FL-Gaussian-O.

**Table 1 Parameters of the light field camera**

| Method | $d_1$ (mm) | $d_2$ (mm) | $f_m$ (mm) | $f$ (mm) | $l_1$ (mm) | $l_m$ (mm) | $P_m$ (mm) | $P_x$ (μm) |
|---|---|---|---|---|---|---|---|---|
| Fahringer's method | - | 0.6 | 0.6 | 100 | 200 | 199.4 | 0.1045 | 5.5 |
| Gaussian method | 10.7996 | 0.5684 | 0.6 | 100 | 200 | 189.2004 | 0.1045 | 5.5 |

### *4.1 Validation of the weight matrix*

In Elsinga's research, the variable $\sigma$ in equation (9) was considered to be a constant, which is very convenient for the calculation of the weight matrix [9]. Since the pixel's line-of-sight in the light field camera has the better representative direction than that in the conventional camera, $\sigma$ is also set as a constant to calculate the weight matrix in light field PIV. In the Tomo-PIV, the reconstructed particle is characterized by a 3D Gaussian-type blob. The size of the 3D Gaussian-type blob should be greater than 3 voxels, ensuring that the 3D cross-correlation algorithm reaches the sub-voxel accuracy level [9]. To achieve the 3×3 Gaussian distribution, $\sigma$ is set as 0.05 in this paper.

The weight matrix by Gaussian function method is compared with those by the theoretical calculation and Fahringer's method to validate its accuracy. Firstly, the theoretical contribution of the voxel to each pixel in the CCD sensor (named as the point spread function (PSF)) is calculated. Fig. 4 shows the schematics of the theoretical calculation of the PSF. In Fig. 4, the voxel is discretized into the point sources (marked as the black spots in Fig. 4). The dense rays (marked as the yellow lines in Fig. 4) from each point source are traced to the main lens, the MLA and the CCD plane, and then imaged on the CCD sensor, shown in Figs. 5(a) and 6(a).

Secondly, for the calculation of the PSF by Fahringer's method and Gaussian function method, $W_{:,j}$ (the $j^{\mathrm{th}}$ column of $W_{m,n}$) is extracted from the whole weight matrix $W$, and then converted to the 2D light field image. Figs. 5 and 6 show the PSF patterns of a single voxel by the theoretical calculation, Fahringer's method and Gaussian function method at $Z$=-5 mm, respectively. From Figs. 5 and 6, the PSF patterns by Fahringer's method and Gaussian function method are closely similar to that by the theoretical calculation at $Z$=-5 mm.

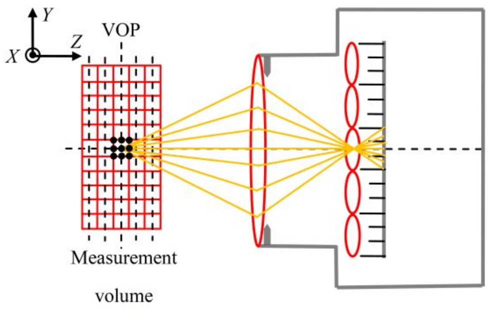


(a)Fahringer's method

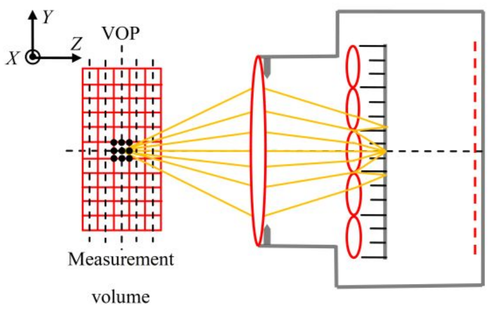


(b)FL

**Fig. 4 Schematics of the theoretical calculation of the PSF**

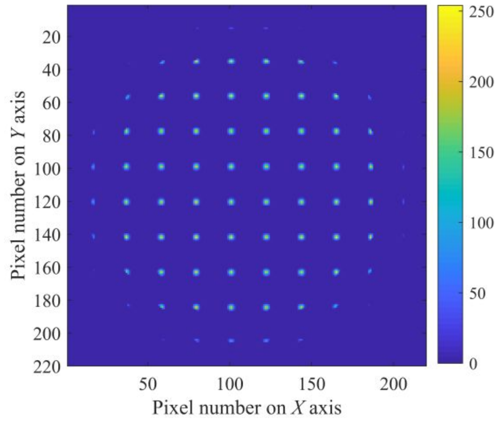


(a)Theoretical calculation

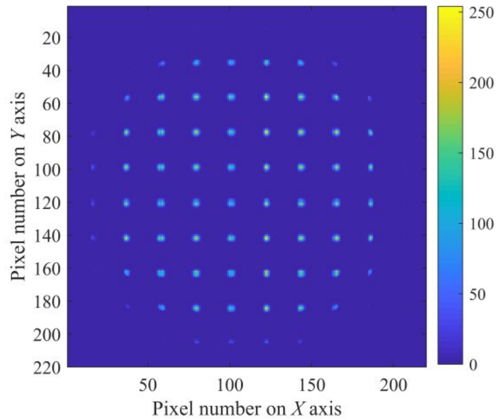


(b) Fahringer's method

**Fig. 5 PSFs of a single voxel of Fahringer's method at *Z*=-5 mm**

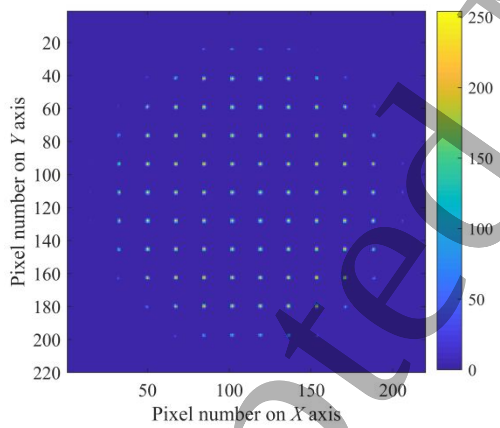


(a)Theoretical calculation

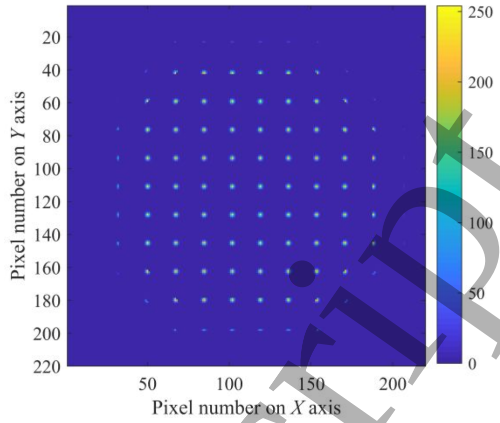


(b) Gaussian function method

**Fig. 6 PSFs of a single voxel of the FL at *Z*=-5 mm**

The Structural Similarity (SSIM) is used to evaluate the similarity of the PSF between the theoretical calculation and the Gaussian function, which is expressed as [53]

$$\mathrm{SSIM}(I_x, I_y) = \frac{(2\mu_x\mu_y + c_1)(2\sigma_{xy} + c_2)}{(\mu_x^2 + \mu_y^2 + c_1)(\sigma_x^2 + \sigma_y^2 + c_2)} \tag{10}$$

where $I_x$ and $I_y$ are the images, SSIM is the similarity between the images $I_x$ and $I_y$, $\mu_x$ and $\mu_y$ are the intensity averages of the images $I_x$ and $I_y$, respectively, $\sigma_x^2$ and $\sigma_y^2$ are the variances of the images $I_x$ and $I_y$, respectively, $\sigma_{xy}$ is the covariance of the images $I_x$ and $I_y$, $c_1$=($k_1L$) and $c_2$=($k_2L$) are the variables to stabilize the division with the weak denominator, $L$ is the dynamic range of the pixel value in the image, and $k_1$=0.01 and $k_2$=0.03. The larger SSIM, the better similarity between the two images. The maximum of SSIM is 1, meaning that the two images are completely the same.

Fig. 7 shows the comparisons of the SSIMs of the PSFs by the theoretical calculation, Fahringer's method and Gaussian function method when the voxel position ranges from -7.5 mm to 7.5 mm. From Fig. 7, the SSIMs of Fahringer's method are better than 0.997 and 0.998 at $Z$=[-7.5, 7.5] mm, respectively, indicating that the PSFs by Fahringer's method are very close to the theoretical PSFs. The SSIMs of the FL are better than 0.998 at $Z$=[-7.5, 2.5] mm, and decreases when the voxel position ranges from 2.5 mm to 7.5 mm. But the SSIIMs of the FL are still better than 0.992 at $Z$=[2.5, 7.5] mm. This validates the feasibility of Gaussian function for the calculation of the weight matrix at $\sigma$=0.05.

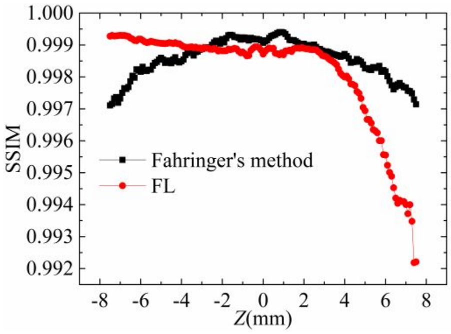


**Fig. 7 Comparisons of the SSIMs by Fahringer's method and Gaussian function method**

The calculation times of the weight matrix at the different numbers of voxels by Fahringer's method and Gaussian function method are compared and summarized in Table 2. The calculated weight matrix needs to be saved in the computer hard disk for Fahringer's method and Gaussian function method. Thus, the overall calculation time of the weight matrix includes the calculation and storage time of the weight matrix.

**Table 2 Calculation times of the weight matrix**

| The number of voxels | *W* by Fahringer's method | *W* by Gaussian function |
|---|---|---|
| 117×117×117 | 19392 s | 1747 s |
| 207×307×167 | 250777 s | 3012 s |
| 207×307×207 | 302852 s | 5214 s |

From Table 2, the overall calculation times of the weight matrix by Fahringer's method and Gaussian function method increase with the increase of the number of voxels. When the number of voxels ranges from 207×307×167 to 207×307×207, the overall calculation time of the weight matrix by Fahringer's method exceeds 2 days, which is very time-consuming. However, Gaussian function method takes thousands of seconds to calculate the weight matrix. This is significantly meaningful for the improvement of the computational efficiency of the weight matrix.

## *4.2 Comparisons of the reconstruction*

In this section, the tracer particles are randomly positioned in a 11.7×11.7×11.7 $mm^3$ volume with 117×117×117 discretized voxels. Fig. 8 shows the comparisons of the reconstruction quality ($Q$) by Multiplicative Algebraic Reconstruction Technique (MART) and EM algorithm. From Fig. 8, EM algorithm can quickly converge to a stable value ($Q$=0.37) within 100 iterations while MART algorithm needs more than 600 iterations to reach a stable value ($Q$=0.35). The calculation times of EM algorithm and MART algorithm are 3050s and 157710s (43.8h), respectively. Thus, EM algorithm is used for the reconstruction of the 3D particle field.

In section 4.2.1, the comparisons of the reconstruction time by EM without SLOS between Gaussian function method and Fahringer's method at different particle concentrations are conducted. In section 4.4.2, the comparisons of the calculation time of the weight matrix including SLOS and the reconstruction (EM including SLOS, SLOS-EM), reconstruction quality at different particle concentrations and velocity field accuracy are carried out.

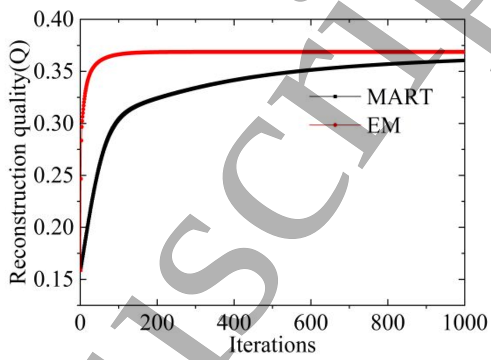


**Fig. 8 Comparisons of the reconstruction quality ($Q$) by MART and EM algorithms**

### *4.2.1 Reconstruction by EM without SLOS*

Fig. 9 shows the synthetic light field images of 200 tracer particles by the FL, respectively. EM without SLOS algorithm is used for the reconstruction of the light field image of Fig. 9. Fig. 10 shows the reconstructed 3D particle fields using Fahringer's method and Gaussian function method corresponding to Fig. 9. From Figs. 10 (b) and (c), the reconstructed 3D particle field by Gaussian function method is almost the same as that by Fahringer's method. The reconstructed particles are all elongated along the $Z$-axis (the depth direction), compared with the predetermined particle distribution in Fig. 10 (a). Note that Gaussian function method can't reduce the elongation of the reconstructed particles.

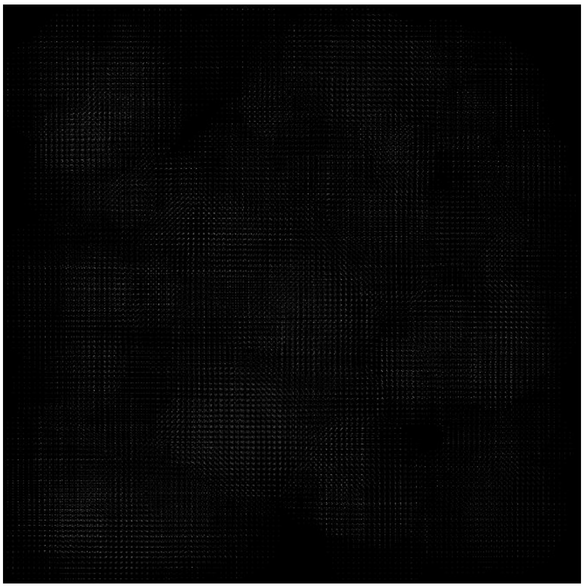

**Fig. 9 Synthetic light field images of 200 tracer particles of FL**

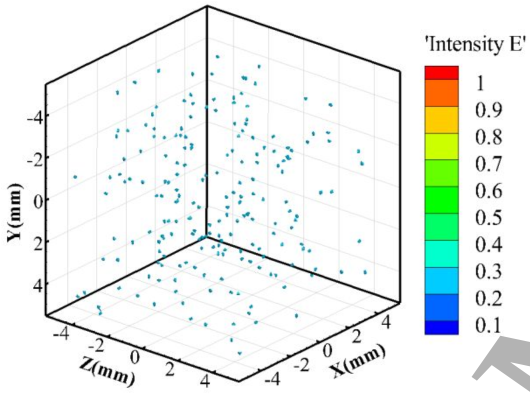


(a)Pre-determined 3D particle field distribution

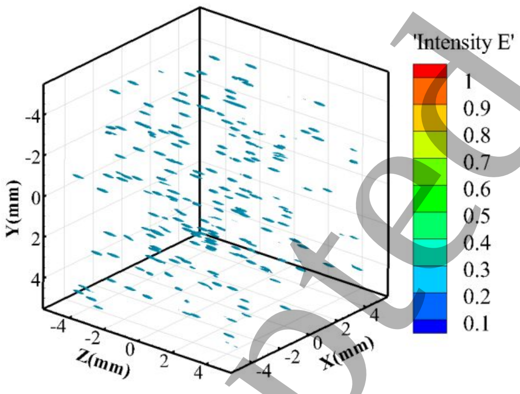


(b)Fahringer's method

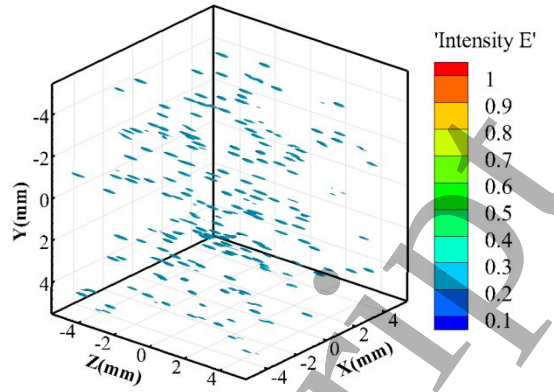


(c) FL-Gaussian

**Fig. 10 Reconstructed 3D particle fields corresponding to Fig. 9**

In reconstruction process of EM without SLOS, the weight matrix is required to read from the computer hard disk. Thus, the overall reconstruction time includes the reading time of the weight matrix from the computer hard disk and reconstruction time of EM without SLOS. Fig. 11 shows the comparisons of the overall reconstruction times of EM without SLOS by Fahringer's method and FL-Gaussian at different particle concentrations. From Fig. 11, the overall reconstruction time of Fahringer's method and FL-Gaussian increases with increasing particle concentration. The overall reconstruction times of EM without SLOS by Gaussian function method are almost the same as that by Fahringer's method. This is because the overall reconstruction process of EM without SLOS by Gaussian function method is exactly the same as that by Fahringer's method. The calculation methods of weight matrix have little effect on the reconstruction time. From Table 2, the overall calculation time of the weight matrix is 1747s when the number of voxels is 117×117×117. From Fig. 11, the overall reconstruction time by EM without SLOS is about 2750s when the particle concentration is 1 ppm. It takes a total of about 4497s (1747+2750) to complete all the process including the calculation, the storage and reading of the weight matrix, and the reconstruction. The whole weight matrix is required to calculate only once and saved in the computer hard disk in advance. For the complex flow, this time-consuming reconstruction is limited to the reconstruction of the particle field at the high concentration of tracer particles. The main reason for the time-consuming reconstruction is that the weight matrix is very large and usually takes up hundreds of GB disk storages [32].

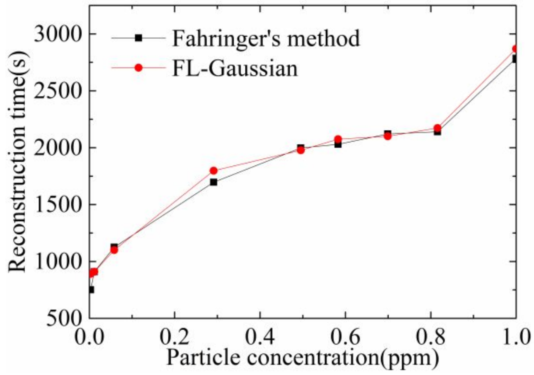


**Fig. 11 Comparisons of the overall reconstruction times of EM without SLOS by Fahringer's method, and FL-Gaussian at different particle concentrations**

*4.2.2 Reconstruction by SLOS-EM*

Research has shown that the tracer particles are sparsely distributed in the measurement volume [54]. Thus, only a small portion of the voxels in the measurement volume has tracer particles, which are defined as the non-zero voxel. For example, when the particle concentration is 1 ppm, there are 13689 tracer particles in the 1601613 discretized voxels, accounting for about 0.85% of the total voxels. As a consequence, the weight matrix is very sparse. So, if the non-zero voxels can be pre-determined, it is useful to further improve the calculation efficiency and the memory storage of the weight matrix and to accelerate the reconstruction process.

A Multiplied line-of-sight (MLOS) estimation has been proposed to pre-determine the non-zero voxels by Atkinson in the conventional Tomo-PIV, and then only the contribution of the non-zero voxels to the pixel is calculated and saved, greatly decreasing the number of the element of the weight matrix [54]. The method has been proved to be efficient to accelerate the reconstruction. In their research work, the pre-determination of the non-zero voxels is that if the intensity of one of the pixels which are affected by the same voxel is equal to 0, this voxel intensity is equal to 0. Thus, the non-zero voxel in the measurement volume is distinguished by multiplying the pixels affected by the same voxel (named as the multiplicative operator).

Fig. 12 shows the non-zero pixel's line-of-sights distribution traced from the light field image of a single particle at ($X$, $Y$, $Z$)=(0, 0, 5) mm. For the light field camera, the multiplicative operator of MLOS is not suitable for the backward ray-tracing technique because the non-zero pixel's line-of-sights (marked as the blue line in Fig. 12) don't fall precisely a single voxel (marked as the yellow rectangle in Fig. 12). $I_t$ is defined as the sum of the number of the total pixel's line-of-sights (includes the zero and the non-zero pixels) accepted by a single voxel. From Fig. 12, note that most of the non-zero pixel's line-of-sights from the light field image of a single particle still fall on the same voxel at $Z$=5mm. As a consequence, when the sum of the number of the non-zero pixel's line-of-sights ($I_a$) accepted by the same voxel is larger than a threshold ($I_a$>0.6$I_t$), this voxel is a non-zero voxel. This pre-determination of the non-zero voxel is named as the summed line-of-sight (SLOS) estimation.

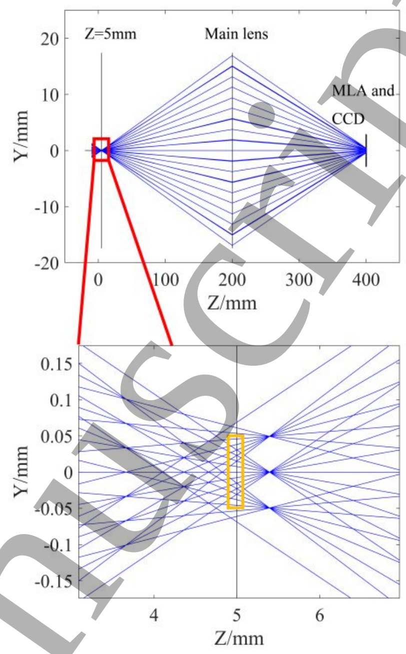


**Fig. 12 Non-zero pixel's line-of-sights distribution traced from the light field image of a single particle at ($X$, $Y$, $Z$)=(0, 0, 5) mm**

The SLOS estimation includes 5 steps. Step 1: all the pixel's line-of-sights including the zero and the non-zero pixels are calculated by the backward ray-tracing technique. Step 2: the pixels affected by the same voxel is determined, and then the sum of the number of the zero and the non-zero pixel's line-of-sights accepted by the same voxel ($I_t$) is calculated. Step 3: According to the light field image, the sum of the number of the non-zero pixel's line-of-sights affected by the same voxel ($I_a$) is calculated. When $I_a$>0.6$I_t$, each non-zero voxel in the discrete volume is distinguished. Step 4: Based on the non-zero voxels determined by SLOS, the contribution of the non-zero voxels to the pixels ($W_{i,j}$) is calculated. Step 5: Reconstruction. The flow chart of the reconstruction in combination with SLOS is shown in Fig. 13

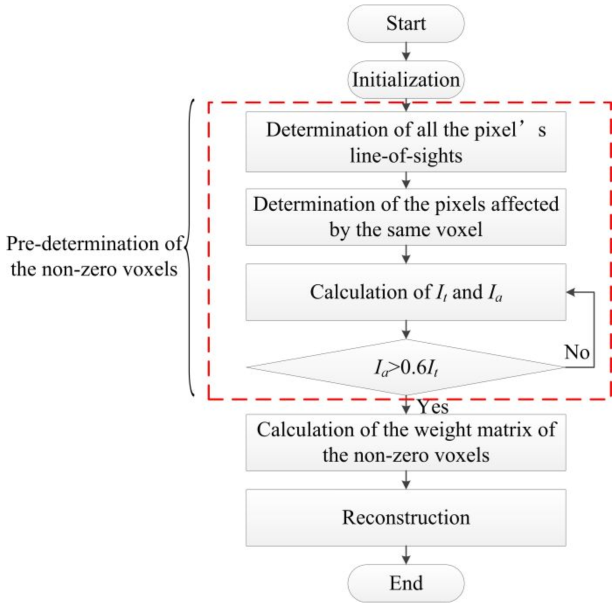


**Fig. 13 Flow chart of the reconstruction including SLOS**

Fig. 14 shows the calculation times of the pre-determination, the weight matrix including SLOS and the reconstruction (EM including SLOS, SLOS-EM). Compared with the reconstruction process of EM without SLOS, the weight matrix including SLOS is not saved in the computer hard disk. From Fig. 14, with increasing the particle concentration, the computation times of the pre-determination, the weight matrix including SLOS and SLOS-EM increase. At the particle concentration of 1 ppm, the calculation times of the pre-determination, the weight matrix including SLOS and SLOS-EM are within 75s, 650s and 275s, respectively. It takes a total of about 1000s (75+650+275) to complete the reconstruction process including the pre-determination, the calculation of the weight matrix and the reconstruction. Compared with Table 2 and Fig. 11, at the particle concentration of 1 ppm, the calculation time of the weight matrix including SLOS (650s) is shorter than that without SLOS (1747s). The reconstruction time of EM including SLOS (275s) is shorter than that without SLOS (2750s). The overall process time including SLOS (1000s) is shorter than that without SLOS (4497s). This indicates that SLOS for the pre-determination of the non-zero voxels is capable of accelerating the computational efficiency of the weight matrix and the reconstruction process, although the weight matrix needs to be recalculated in each reconstruction.

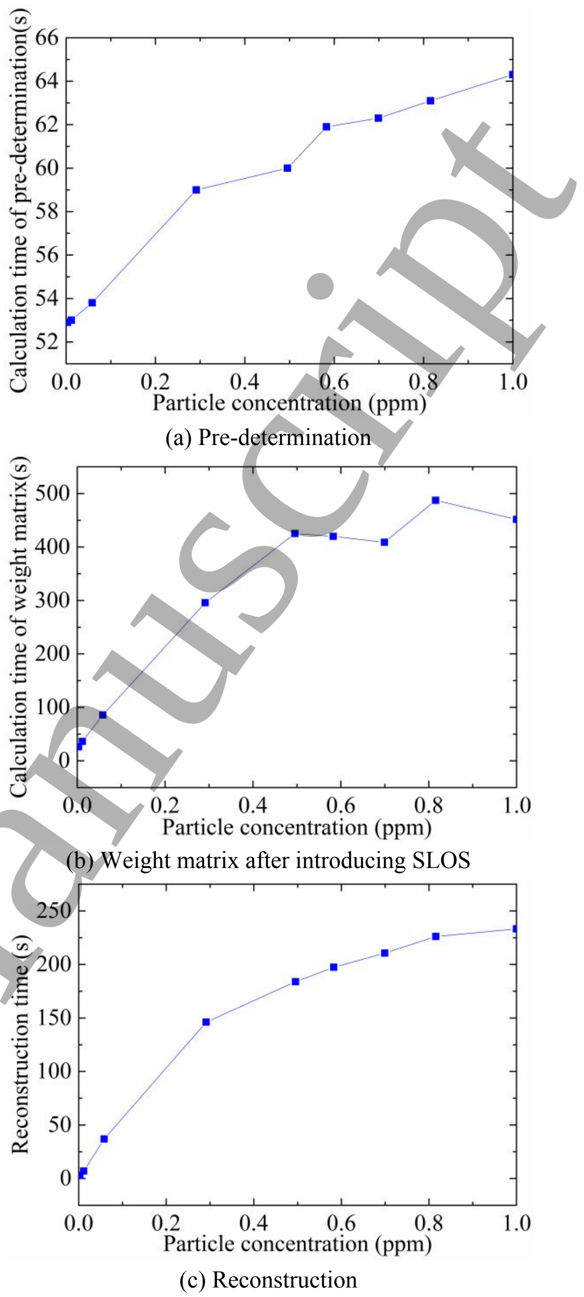


**Fig. 14 Calculation times of the pre-determination, the weight matrix including SLOS and the reconstruction (EM including SLOS, SLOS-EM)**

The effects of the MLA arrangement and SLOS on the reconstruction quality at different particle concentrations are also investigated. The reconstruction qualities of Fahringer's method, FL-Gaussian-O, FL-Gaussian-H, and FL-Gaussian-SLOS at different particle concentrations are compared in Fig. 15. It can be seen that in all cases, the reconstruction quality decreases with the increase of the particle concentration for the light field PIV. The reconstruction qualities of Gaussian function method are almost consistent with those of Fahringer's method. It can be concluded that the introduction of SLOS has little effect on the reconstruction quality, but is capable of improving the computation efficiency of the reconstruction. In addition, Gaussian function method is also suitable for the calculation of the weight matrix in the MLA of the hexagonal arrangement.

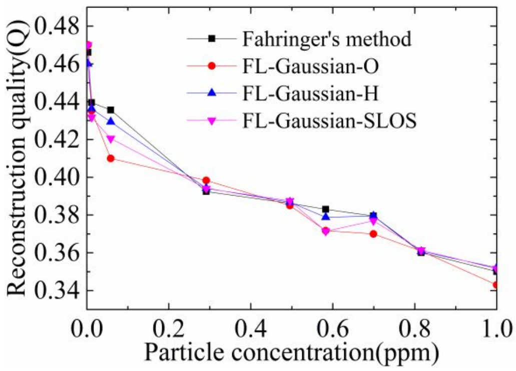


**Fig. 15 Reconstruction quality at different particle concentrations**

The measurement accuracy of the velocity field is mostly concerned in the PIV. A simulation of the laminar flow is used to further validate the feasibility and accuracy of the weight matrix by Gaussian function method. The tracer particles with the concentration of 1 ppm are randomly distributed in a 11.7×11.7×11.7 mm$^3$ volume. The laminar velocity is 0.02 m/s. In simulation, a pair of the synthetic light field images is firstly generated by the forward ray-tracing technique. The time interval $\Delta t$ between the pairs of light field images is 16 ms. The 3D particle fields of the laminar flow are then reconstructed from the synthetic light field images, and finally the 3D velocity field of the laminar flow is calculated by the 3D cross-correlation algorithm. The interrogation window of 3D cross-correlation is set as 16×16×16 with 50% overlap of the interrogation windows. Fig. 16 shows the theoretical and calculated 3D velocity fields of the laminar flow. The theoretical 3D velocity field of the laminar flow in Fig. 16 (a) is

$$v(y) = v_{\mathrm{m}}[1-(\frac{y}{R})^2] \quad (11)$$

where $v_{\mathrm{m}}$ is the maximum velocity of the laminar flow, $R$ is the size of the pipe, and $y$ is the coordinate on the $Y$-axis.

Fig. 17 shows the comparisons of 1D velocity distributions of the laminar flow. It can be seen from Figs. 16 and 17 that the 3D velocity field by FL-Gaussian-O is consistent with the theoretical velocity field. The 3D velocity fields by FL-Gaussian-H and FL-Gaussian-SLOS are almost the same as the theoretical velocity field, and are not illustrated here. The 1D velocity distributions of the laminar flow by Fahringer's method and Gaussian function method are parabolic and in good agreement with the theoretical velocity. Fig. 18 shows relative errors of the 1D velocity distributions. From Fig. 18, the relative errors of the 1D velocity distributions by all the cases are within 5%. The relative errors near the edge of the measurement volume are slightly larger than that near the centre of the measurement volume. This is because of the lack of the velocity information at the edge of the flow field, which is unbeneficial for the interpolation calculation of 3D cross-correlation.

The correlation coefficient is further used to evaluate the similarity between the simulation and theoretical 1D velocity distribution, which is expressed as

$$R(a,b) = \frac{\mathrm{Cov}(a,b)}{\sigma_a \sigma_b} \quad (12)$$

where Cov($a$, $b$) is the covariance of variables $a$ and $b$, and $\sigma_a$ and $\sigma_b$ are the standard deviations of $a$ and $b$, respectively.

Table 3 shows the results of the correlation coefficient. The correlation coefficients by Fahringer's method and Gaussian function method are all more than 0.99, which is very close to 1. This further indicates that the velocity fields by Fahringer's method and Gaussian function method are almost the same as the theoretical velocity field.

It is concluded that the weight matrix by Gaussian function method can be used for the accurate measurement of the 3D velocity field in the light field PIV. What's more, Gaussian function method has higher computational efficiency of the weight matrix than Fahringer's method.

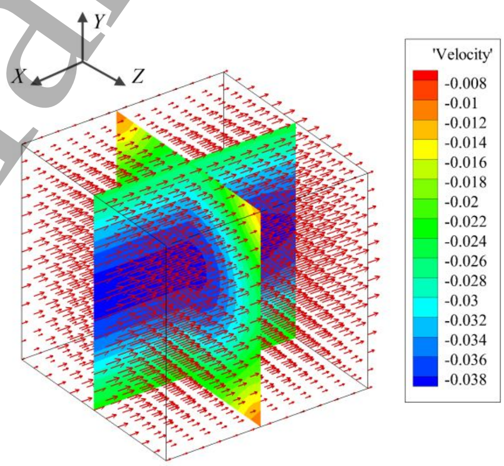


(a)Theoretical 3D velocity field

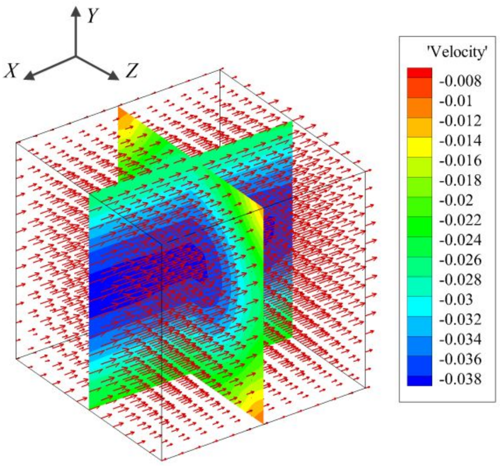


(b)3D velocity field by FL-Gaussian-O

**Fig. 16 Theoretical and calculated 3D velocity fields of the laminar flow**

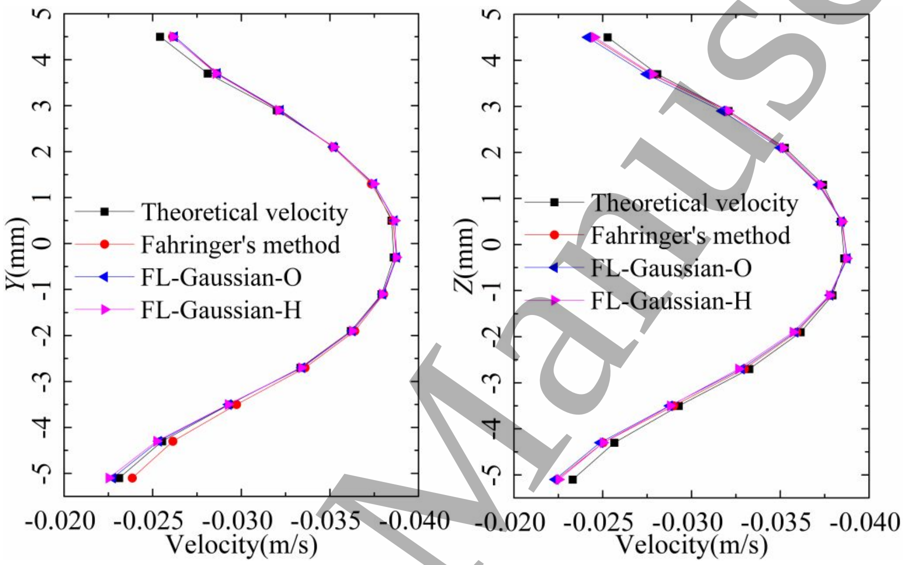


(a)*XOY* plane at *Z*=-0.13mm (b) *XOZ* plane at *Y*=-0.13mm

**Fig. 17 Comparisons of 1D velocity distributions of the laminar flow**

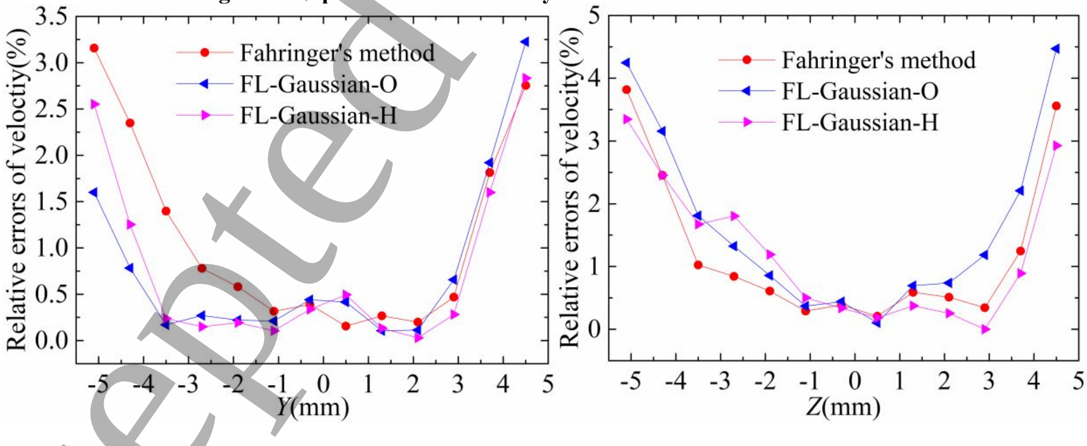


(a)*XOY* plane at *Z*=-0.13mm (b) *XOZ* plane at *Y*=-0.13mm

**Fig. 18 Relative errors of 1D velocity distributions**

**Table 3 Results of the correlation coefficient**

| | **Fahringer's method** | **FL-Gaussian-O** | **FL-Gaussian-H** |
|---|---|---|---|

| | | | |
|---|---|---|---|
| Fig. 17 (a) | 0.9997 | 0.9998 | 0.9994 |
| Fig. 17 (b) | 0.9998 | 0.9985 | 0.9983 |

## 5. Experimental verification

Experiments are further conducted to verify Gaussian function method for the calculation of the weight matrix. Fig. 19 shows the experimental rig of the light field PIV in our group. It is mainly comprised of the assembled light field PIV and the laminar flow rig. The assembled light field PIV, as shown in Fig. 19 (a), includes one double pulsed laser source, one focused light field camera (Raytrix R29) and one synchronous controller. The optical parameters of Raytrix R29 are calibrated using Sun's and Strobl's calibration method, and summarized in Table 4 [55-56]. From Table 4, the MLA of the Raytrix R29 has three microlenses with different focal lengths. The inaccurate optical parameters of light field camera such as the lens distortion, the MLA offset, the image distance, the distance between CCD and MLA *etc.* would affect the accuracy of the reconstructed particle position. The lens distortion has been considered in the Sun's and Strobl's calibration method. What's more, the MLA offset is corrected by Raytrix R29 software. Thus, Raytrix R29 software is capable of providing the accurate light field image and total focused image for calibration. According to calibrated optical parameters of Raytrix R29, the depth accuracy has been verified by reconstructing the pinhole position in our previous work [37]. Our previous validation work showed that the optical parameters of Raytrix R29 by Sun's and Strobl's calibration method are capable of reconstructing an accurate particle position.

Fig. 19 (b) shows a schematic of the laminar flow rig, including two reservoirs, two valves, a flow meter and a submersible pump. The acrylic channel is a 15mm×15mm square with a length of 2000 mm. Purified water is pumped from the reservoir 1 into the reservoir 2 by the submersible pump, and flows into the reservoir 1 along the acrylic channel. To make the flow stable in measurement volume, the valves 1 and 2 are regulated to keep a constant water level in the reservoir 2. The flow field is seeded with polyamide particles with a mean diameter of 50 μm, a density of 1.03 g/cm$^3$ and a particle concentration of 0.89 ppm. Illumination is provided by a Vlite 200 double pulsed laser source with the maximum output energy of 200 mJ per pulse at 532 nm and a pulse duration of 7 ns.

The flowrate is 0.3 L/min in the experiment, and the corresponding average velocity and the Reynolds number (ReD) in the channel are 0.0222 m/s and 387, respectively. The measurement volume is 30mm (*X*-axis) × 15mm (*Y*-axis) × 15mm (*Z*-axis), and discretized into 300×150×150 voxels. The 3D cross-correlation window size is 64×64×64 with 85% overlap of interrogation windows.

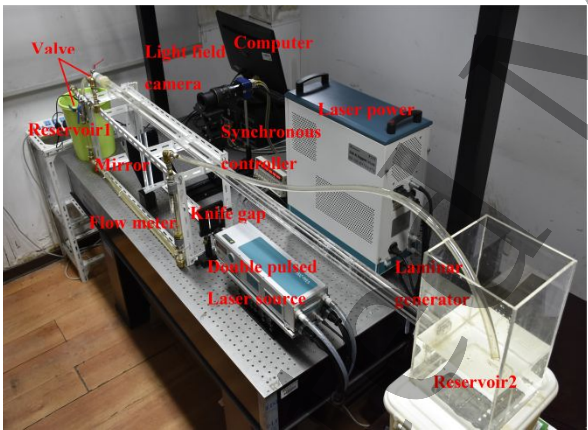


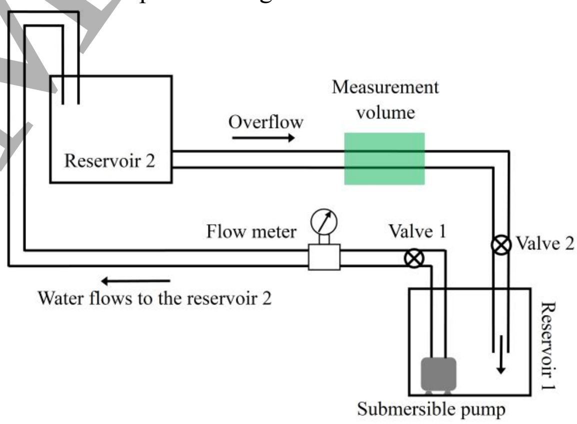


(a)Schematic of the experimental setup of the assembled light field PIV (b)Laminar flow rig

**Fig. 19 Experimental rig of the light field PIV**

**Table 4 Parameters of the Raytrix R29**

| $d_1$ (mm) | $d_2$ (mm) | $f_m$ (mm) | $f$ (mm) | $l_1$ (mm) | $l_m$ (mm) | $P_m$ (mm) | $P_x$ (μm) |
|---|---|---|---|---|---|---|---|
| 10.2903 | | 1.3474 | | | | | |
| 4.4447 | 1.1914 | 1.6277 | 100 | 193.7112 | 195.2292 | 0.1705 | 5.5 |
| 2.8496 | | 2.0474 | | | | | |

Fig. 20 shows the raw light field images of the laminar flow with tracer particles. From Fig. 20, the pixels under each microlens are highlighted to form a series of sub-images that are the hexagonal arrangement. Fig. 21 shows the 3D-3C velocity field and 2D velocity distributions of the laminar flow. Figs. 21 (b), (c), and (d) show the 2D velocity distributions at five *YOZ* planes (*X*=-10.95mm, -5.55mm, -0.15mm, 5.25mm and 10.65mm), one *XOY* plane (*Z*=0.15 mm) and one *XOZ* plane (*Y*=0.15 mm), respectively. From Fig. 21, the flow moves in the negative direction along the *X*-axis. The maximum velocity of the laminar flow is 0.042 m/s near the center of the channel. The corresponding average velocity is 0.028 m/s, which is very close to the theoretical average velocity of 0.0222 m/s.

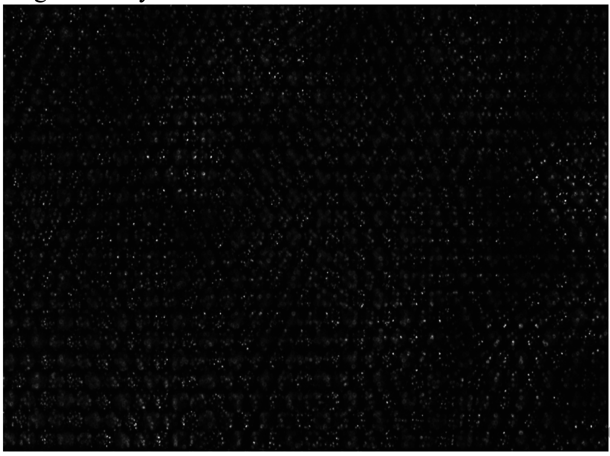

(a)First frame

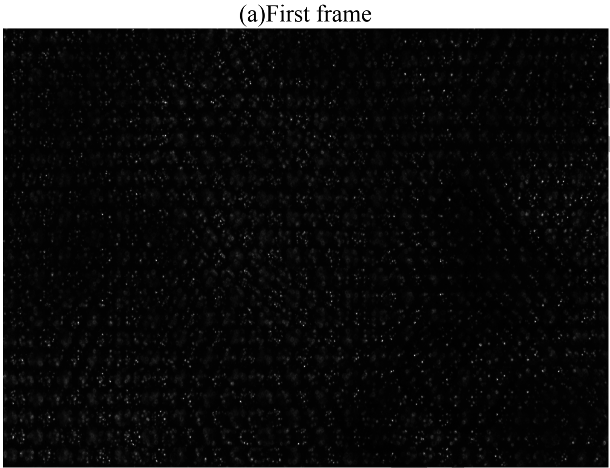

(b) Second frame

**Fig. 20 Raw light field images of the laminar flow with the tracer particles**

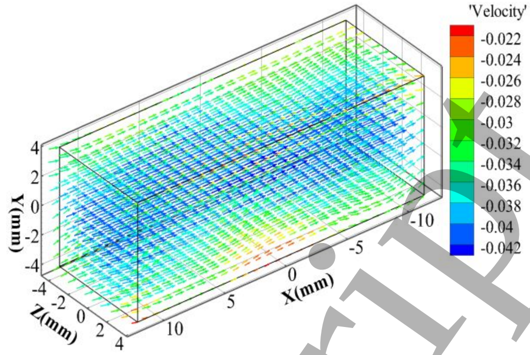


(a)3D velocity field

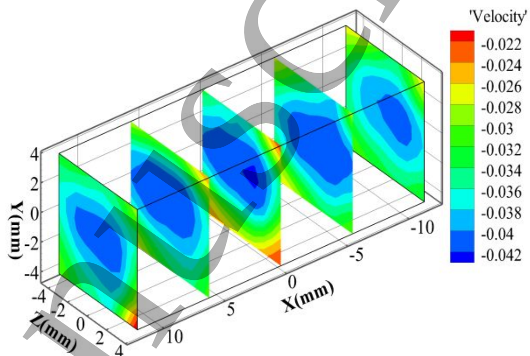


(b) 2D velocity distribution at *YOZ* plane

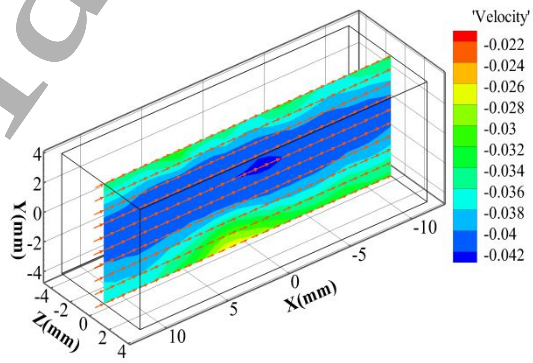


(c) 2D velocity distribution at *XOY* plane

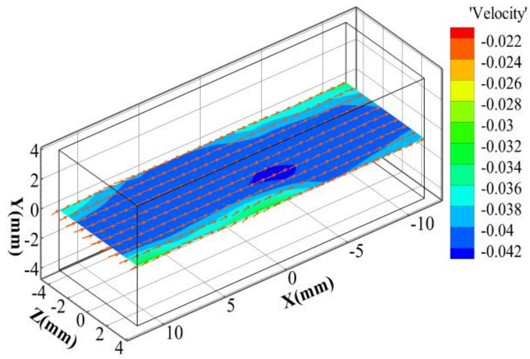


(d) 2D velocity distribution at *XOZ* plane

**Fig. 21 3D-3C velocity field and 2D velocity distributions of the laminar flow**

Fig. 22 (a) shows the 1D velocity distributions vary with the *Y*-axis at *XOY* plane corresponding to Fig. 21 (c). Fig. 22 (b) shows the 1D velocity distributions vary with the *Z*-axis at *XOZ* plane corresponding to Fig. 21 (d). From Fig. 22, all the 1D velocities along the *Y*-axis and the *Z*-axis have parabolic distributions, and their profiles are fairly good agreement with the theoretical velocity. The 1D velocity distributions in Fig. 22 (b) at *Z*=[-2, 2] mm is flat, which is caused by the low depth resolution of the Raytrix R29 in the *Z*-axis. The velocities in all the cases are slightly slower than the theoretical velocities. Note that the velocities near the wall of the acrylic channel are slower than those near the centre of the acrylic channel in all the 1D velocity distributions, which is caused by the viscosity of the fluid. What's more, the velocities near the center of the acrylic channel is closer to the theoretical velocities than those near the wall of the acrylic channel, which is mainly attributable to the surface roughness of the wall of the acrylic channel. The surface roughness further slows down the velocity of the tracer particles near the wall of the acrylic channel. Fig. 23 shows relative errors of the 1D velocity distributions. It can be seen that the velocity errors near the center of the acrylic channel are within 8%, which is acceptable and consistent with the published research [57]. Table 5 shows results of the correlation coefficient corresponding to Fig. 22. The correlation coefficients of the 1D velocities along the *Y*-axis is better than that along the *Z*-axis. Overall, these experimental results further verify the feasibility of the weight matrix by the backward ray-tracing technique in combination with Gaussian function. The weight matrix by Gaussian function method is capable of measuring the instantaneous 3D-3C velocity field.

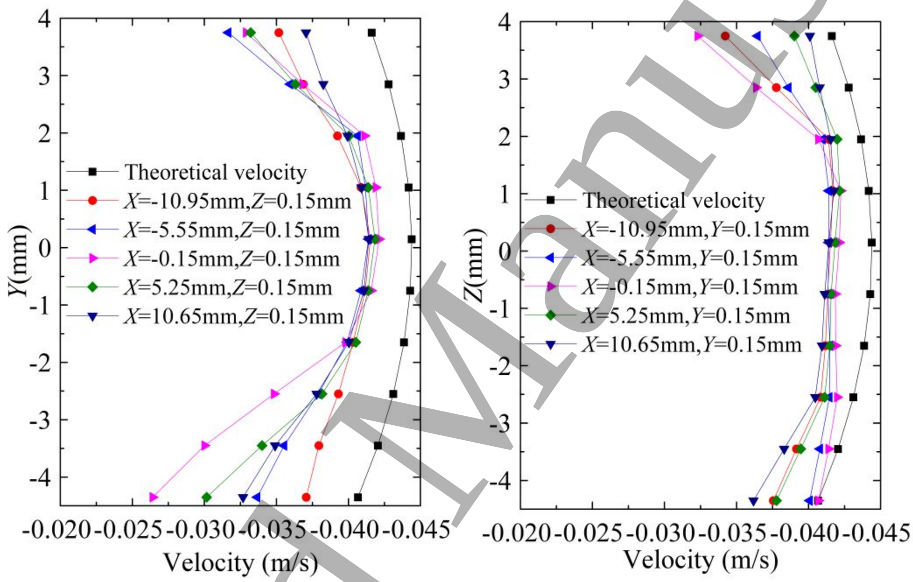


(a) 1D velocity distributions corresponding to Fig. 21 (c) (b) 1D velocity distributions corresponding to Fig. 21 (d)

**Fig. 22 1D velocity distributions of the laminar flow**

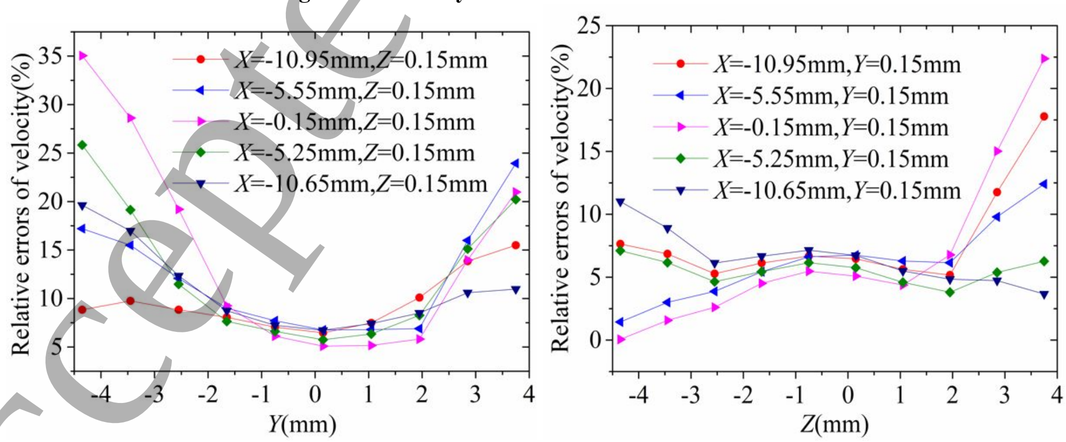


(a) 1D velocity distributions corresponding to Fig. 22 (a) (b) 1D velocity distributions corresponding to Fig. 22 (b)

**Fig. 23 Relative errors of the 1D velocity distributions**

**Table 5 Results of the correlation coefficient**

| | *X*=-10.95 mm | *X*=-5.55 mm | *X*=-0.15 mm | *X*=5.25 mm | *X*=10.65 mm |
|---|---|---|---|---|---|
| Fig. 22 (a) | 0.8823 | 0.9277 | 0.9608 | 0.9965 | 0.9626 |
| Fig. 22 (b) | 0.7143 | 0.5793 | 0.5004 | 0.9735 | 0.9483 |

## 6.Conclusions

In this paper, a backward ray-tracing technique in combination with Gaussian function was proposed to calculate the weight matrix of the light field PIV and to improve its computational efficiency. An Expectation-Maximization (EM) algorithm in combination with SLOS estimation was further employed to accelerate the reconstruction of the tracer particle field. Numerical simulations were carried out to investigate the computational accuracy and efficiency of the weight matrix, the reconstruction quality of the tracer particles field, and the accuracy of the 3D velocity field. Experiments have been also conducted to measure the 3D-3C velocity field of a laminar flow. Simulation results showed that the calculation time of the weight matrix by Gaussian function method is better than that by Fahringer's method. SLOS estimation is capable of improving the reconstruction efficiency, and has no effect on the reconstruction quality. Meanwhile, the reconstructed quality and the velocity field accuracy by Gaussian function method are almost similar to those by Fahringer's method. Experiment results further proved the feasibility of the weight matrix by Gaussian function method.

## Acknowledgements

The authors wish to express their gratitude to the National Natural Science Foundation of China (No. 51676044).

## References

[1] Arroyo M P, Hinsch K D 2007 Recent developments of PIV towards 3D measurements *Particle image velocimetry, Springer, Berlin, Heidelberg* 127-154

[2] Cierpka C, Kähler C J 2012 Particle imaging techniques for volumetric three-component (3D3C) velocity measurements in microfluidics *Journal of visualization* 15(1) 1-31

[3] Wang J X, Li Y Z, Li J X, *et al* 2019 A gas-atomized spray cooling system integrated with an ejector loop: Ejector modeling and thermal performance analysis *Energy conversion and management* 180 106-118

[4] Scarano F, Poelma C 2009 Three-dimensional vorticity patterns of cylinder wakes *Experiments in Fluids* 47(1) 69

[5] De Silva C M, Baidya R, Khashehchi M, *et al* 2012 Assessment of tomographic PIV in wall-bounded turbulence using direct numerical simulation data *Experiments in fluids* 52(2) 425-440

[6] Violato D, Scarano F 2011 Three-dimensional evolution of flow structures in transitional circular and chevron jets *Physics of Fluids* 23(12) 124104

[7] Salah R B, Alata O, Thomas L, *et al* 2014 3D particle volume tomographic reconstruction based on marked point process: Application to tomo-piv in fluid mechanics *IEEE International Conference on Acoustics, Speech and Signal Processing (ICASSP)* 8153-8157

[8] Novara M, Scarano F 2012 Performances of motion tracking enhanced Tomo-PIV on turbulent shear flows *Experiments in fluids* 52(4) 1027-1041

[9] Elsinga C E, Scarano F, Wieneke B, *et al* 2006 Tomographic particle image velocimetry *Experiments in Fluids* 41(6) 933-947

[10]Worth N A, Nickels T B, Swaminathan N 2010 A tomographic PIV resolution study based on homogeneous isotropic turbulence DNS data *Experiments in Fluids* 49(3) 637-656

[11]Lynch K, Thurow B 2011 Preliminary development of a 3-D, 3-C PIV technique using light field imaging *41st AIAA Fluid Dynamics Conference and Exhibit* 1-15

[12]Houwelingen J V, Holten A P C, Clercx H J H, *et al.* 2020 Visualizing large-scale fow using synthetic aperture PIV *Experiments in fluids* 1-14

[13]Belden, J, Truscott, T. T, Axiak, M. C, *et al.* 2010 Three-dimensional synthetic aperture particle image velocimetry, *Measurement Science and Technology* 21(12)

[14]Lynch K 2011 Development of a 3-D Fluid Velocimetry Technique based on Light Field Imaging *Auburn University*

[15]Gao Q, Wang H P, Shen G X, *et al* 2013 Review on development of volumetric particle image velocimetry *Science Bulletin* 58(36) 4541-4556

[16]Gao Q, Wang H P, Wang J J 2012 A single camera volumetric particle image velocimetry and its application *Science China Technological Sciences* 55(9) 2501-2510

[17]Lynch K P, Fahringer T W, Thurow B W 2012 Three-dimensional particle image velocimetry using a plenoptic camera *50th AIAA Aerospace Sciences Meeting Including the New Horizons Forum and Aerospace Exposition* 1-14

[18]Fahringer T W, Lynch K P, Thurow B S 2015 Volumetric particle image velocimetry with a single plenoptic camera *Measurement Science and Technology* 26(11) 115201

[19]Shi S X, Ding J F, New T H, Soria J 2017 Light-field camera-based 3D volumetric particle image velocimetry with dense ray tracing reconstruction technique *Experiments in Fluids* 58(7) 78

[20]Shi S X, Xu S M, Zhao Z, *et al* 2018 3D Surface Pressure Measurement with Single Light-Field Camera and Pressure-Sensitive Paint *Experiments in Fluids* 59(5) 79

[21]Georgiev T, Lumsdaine A 2010 Reducing plenoptic camera artifacts *Computer Graphics Forum. Blackwell Publishing Ltd* 29(6) 1955-1968

[22]Ng R, Levoy M, Brédif M, *et al* 2005 Light field photography with a hand-held plenoptic camera *Computer Science Technical Report CSTR* 2(11) 1-11

[23]Skupsch C , Brücker, Christoph 2013 Multiple-plane particle

image velocimetry using a light-field camera *Optics Express* 21(2) 1726-40

[24]Bolton J T , Thurow B S , Alvi F S , *et al* 2017 Single Camera 3D Measurement of a Shock Wave-Turbulent Boundary Layer *Interaction Aiaa Aerospace Sciences Meeting*

[25]Thomason C 2014 Determination of the Image Distance in a Plenoptic Camera *Auburn University*

[26]Munz H E , Fahringer T W , Guildenbecher D R , *et al* 2018 Volumetric calibration of a plenoptic camera *Applied Optics* 57(4) 914

[27]Fahringer T W, Thurow B S 2018 Plenoptic particle image velocimetry with multiple plenoptic cameras *Measurement Science and Technology* 29(7) 1-20

[28]Shi S X, Wang J H, Ding J F, *et al* 2016 Parametric study on light field volumetric particle image velocimetry *Flow Measurement and Instrumentation* 49 70-88

[29]Shi S X, Ding J F, Atkinson C, *et al* 2018 A detailed comparison of single-camera light-field PIV and tomographic PIV *Experiments in Fluids* 59(3) 46

[30] Shi S X , Ding J F, New T H *et al* 2019 Volumetric calibration enhancements for single-camera light-field PIV *Experiments in Fluids* 60(1) 21

[31] Zhao Y Y, Li H T, Mei D , Shi S X 2020 Metric calibration of unfocused plenoptic cameras for three-dimensional shape measurement *Optical Engineering* 59(7) 073104

[32] Mei D, Ding J F, Shi S X, *et al* 2019 High resolution volumetric dual-camera light-field PIV *Experiments in Fluids* 60(8) 132

[33] Ding J F, Xu S M, Zhao Z, Shi S X, *et al* 2019 Volumetric Measurement of Synthetic Jet Impingement with Single-camera Light-field PIV *13th International Symposium on Particle Image Velocimetry – ISPIV* 22-24

[34]Zhao Z , Buchner A J , Ding J F, *et al* 2019 Volumetric Measurements of a Self-similar Adverse Pressure Gradient Turbulent Boundary Layer Using Single-camera Light-field Particle Image Velocimetry *Experiments in Fluids* 60(9):141

[35]Ding J F, Lim H D , Sheikh S , *et al* 2018 Volumetric Measurement of a Supersonic Jet with Single-Camera Light-Field PIV *19th International Symposium on the Application of Laser and Imaging Techniques to Fluid Mechanics*

[36]Ding J F, Li H T, Ma H X, *et al* 2019 A Novel Light Field Imaging Based 3D Geometry Measurement Technique for Turbomachinery Blades *Measurement ence and Technology* 30(11):115901

[37]Cao L X, Zhang B, Li J, *et al* 2019 Characteristics of tomographic reconstruction of light-field Tomo-PIV *Optics Communications* 442 132-147

[38]Fahringer T, Thurow B S 2012 Tomographic reconstruction of a 3-d flow field using a plenoptic camera *42nd AIAA Fluid Dynamics Conference and Exhibit* 2826

[39]Thurow B S, Fahringer T 2013 Recent development of volumetric PIV with a plenoptic camera *10th International Symposium on Particle Image Velocimetry* 1-7

[40]Ding J F, Wang J H, New T H, *et al* 2016 Dense ray tracing based reconstruction algorithm for light-field volumetric particle image velocimetry *18th International Symposium on the Application of Laser and Imaging Techniques to Fluid Mechanics*

[41]Scarano F 2013 Tomographic PIV: principles and practice, *Measurement Science & Technology* 24(1) 012001

[42]Westfeld P, Maas H G, Pust O, *et al* 2010 3-D least squares matching for volumetric velocimetry data processing *Proceedings of the 15th International Symposium on Appliocations of Laser Techniques to Fluid Mechnaics* 5-8

[43]Ziskin I B, Adrian R J, Prestridge K 2011 Volume segmentation tomographic particle image velocimetry *Proceedings of 9th international symposium on particle image velocimetry. Kobe University, Kobe, Japan* 21-23

[44]Thomas L, Tremblais B, David L 2014 Optimization of the volume reconstruction for classical Tomo-PIV algorithms (MART, BIMART and SMART): synthetic and experimental studies *Measurement Science & Technology* 15(3) 035303

[45]Liu G, Siavash Y, Zhi Z, *et al* 2011 Automatic estimation of point-spread-function for deconvoluting out-of-focus optical coherence tomographic images using information entropy-based approach *Optics Express* 19(19) 18135-18148

[46]Sun J, Xu C L, Zhang B, *et al* 2016 Three-dimensional temperature field measurement of flame using a single light field camera *Optics Express* 24(2) 1118-1132

[47]Buchmann N A, Atkinson C, Jeremy M C, *et al* 2011 Tomographic particle image velocimetry investigation of the flow in a modeled human carotid artery bifurcation *Experiments in Fluids* 50(4) 1131-1151

[48] Laasmaa M, Vendelin M, Peterson P 2011 Application of Regularized Richardson–Lucy Algorithm for Deconvolution of Confocal Microscopy Images *Journal of Microscopy* 100(2):139a-139a

[49]Thiébaut, Éric, Thi E 2006 Introduction to image reconstruction and inverse problems *Journal of the Society of Instrument and Control Engineers* 45 726-730

[50]Soriano A, Rodríguezalvarez M J, Iborra A, *et al* 2013 EM tomographic image reconstruction using polar voxels *Journal of Instrumentation* 8(1) C01004

[51]Hojjatoleslami S A, Avanaki M R N, Podoleanu A G 2013 Image quality improvement in optical coherence tomography using Lucy-Richardson deconvolution algorithm *Applied Optics* 52(23) 5663-5670

[52]De Silva C M, Baidya R, Khashehchi M, *et al* 2012 Assessment of tomographic PIV in wall-bounded turbulence using direct numerical simulation data *Experiments in fluids* 52(2) 425-440

[53]Zhou W, Bovik A C, Sheikh H R, *et al* 2014 Image quality assessment: From error visibility to structural similarity *IEEE Transactions on Image Processing* 13(4) 600-612

[54]Atkinson C, Soria J 2009 An efficient simultaneous reconstruction technique for tomographic particle image velocimetry *Experiments in Fluids* 47(4-5) 553-568

[55]Sun J, Hossain M M, Xu C L, *et al* 2017 A novel calibration method of focused light field camera for 3-D reconstruction of flame temperature *Optics Communications* 390 7-15

[56]Strobl K H, Lingenauber M 2016 Stepwise calibration of focused plenoptic cameras *Computer Vision and Image Understanding* 145 140-147

[57]Lima R, Wada S, Tsubota K, *et al* 2006 Confocal micro-PIV measurements of three-dimensional profiles of cell suspension flow in a square microchannel *Journal of Biomechanics* 39(4) 332-332